Downloaded from orbit.dtu.dk on: Apr 26, 2025

DTU Library

Degradation mechanisms of amine-cured epoxy novolac and bisphenol F resins under conditions of high pressures and high temperatures

Rajagopalan, Narayanan; Erik Weinell, Claus; Dam-Johansen, Kim; Kiil, Søren

Published in:
Progress in Organic Coatings

Link to article, DOI:
10.1016/j.porgcoat.2021.106268

Publication date:
2021

Document Version
Peer reviewed version

Link back to DTU Orbit

Citation (APA):
Rajagopalan, N., Erik Weinell, C., Dam-Johansen, K., & Kiil, S. (2021). Degradation mechanisms of amine-cured epoxy novolac and bisphenol F resins under conditions of high pressures and high temperatures. *Progress in Organic Coatings*, *156*, Article 106268. https://doi.org/10.1016/j.porgcoat.2021.106268

General rights
Copyright and moral rights for the publications made accessible in the public portal are retained by the authors and/or other copyright owners and it is a condition of accessing publications that users recognise and abide by the legal requirements associated with these rights.

- Users may download and print one copy of any publication from the public portal for the purpose of private study or research.
- You may not further distribute the material or use it for any profit-making activity or commercial gain
- You may freely distribute the URL identifying the publication in the public portal

If you believe that this document breaches copyright please contact us providing details, and we will remove access to the work immediately and investigate your claim.

Degradation mechanisms of amine-cured epoxy novolac and bisphenol F resins under conditions of high pressures and high temperatures

Narayanan Rajagopalan[*], Claus Erik Weinell[*], Kim-Dam Johansen[*], and Søren Kiil[*, a]

a: Corresponding author, email address: sk@kt.dtu.dk
*: CoaST, Department of Chemical and Biochemical Engineering, Technical University of Denmark, DTU, Building 229, 2800 Kgs. Lyngby, Denmark.

Abstract

Projections of continued growth in the global hydrocarbon demand and fast depleting resources push the oil and gas industry to explore and produce in geological formations with abnormal high pressures and temperatures, so-called HPHT conditions. In the present study, the largely unexplored degradation mechanisms for amine-cured epoxy novolac (EN) and bisphenol F (BPF) epoxy resins at HPHT are investigated at lower limits of HPHT.

Using a batch-like reactor encompassing the three relevant phases (a gas mixture of nitrogen and carbon dioxide, a hydrocarbon phase of aromatic para-xylene, and an artificial seawater phase), the conditions of high pressures and high temperatures were simulated. The EN and BPF coated steel panels were placed inside the batch reactor.

In the gas phase-exposed zone, both EN and BPF remained essentially intact with no major defects. However, due to para-xylene uptake that resulted in a free volume increase (i.e. lowering of the glass transition temperature), the hydrocarbon-exposed zones of EN and BPF were partly covered by an oxide of iron, the origin of which was found to be diffusion of anodically-dissolved iron from the steel-coating interface. The enhanced resin chain mobility at the hydrocarbon-seawater interphase allowed higher rates of diffusion of seawater ions to the steel-coating interface with clear signs of coating degradation. Finally, the seawater phase induced small blisters in the EN coating, whereas for BPF, a complete loss of adhesion between the coating and the substrate was observed.

Simulation of Rapid Gas Decompression (RGD), uncovered the role of RGD in the iron oxide formation process for both EN and BPF coatings.

In summary, when compared to BPF, the EN network showed superior performance under conditions of HPHT.

Keywords: epoxy novolac; epoxy bisphenol F; corrosion; high pressures; high temperatures; coatings;

List of Abbreviations

EN	Amine-cured epoxy novolac resin system
BPF	Amine-cured epoxy bisphenol F resin system
HPHT	High-pressure high temperature
DM	Digital microscopy
SEM	Scanning electron microscopy
EDX	Energy Dispersive X-Ray
ATR-FTIR	Attenuated Total Reflectance – Fourier Transform Infrared
DSC	Differential Scanning Calorimetry
RGD	Rapid gas decompression
DGEBA	Bisphenol A diglycidyl ether
DEAPA	3-(Diethylamino) propylamine
MXDA	m-Xylylenediamine
Amicure PACM	bis-(p-aminocyclohexyl) methane
DFT	Dry film thickness

List of Symbols

T_g	Glass transition temperature

1. Introduction

Renewable energy sources have grown remarkably in the past ten years. However, fossil fuels will remain the primary resource for meeting the global energy demand. Moreover, on all continents, the rapid depletion of oil reserves has pushed the oil and gas industry to focus on geological formations with abnormal high pressure and high temperature conditions [1].

For half a century, the oil and gas industry has been challenged with the definition of elevated temperatures and pressures, but no industry standards that define the interrelationship between temperature and pressure have been registered. One of the most common HPHT definitions is when the pressure exceeds 690 bars (10,000 psi) and/or the temperature exceeds 149 ^{o}C (300 °F) [1-3]. The US Code of Federal regulations and the American Petroleum Institute (API) established similar pressure and/or temperature ratings to classify the conditions as HPHT [2, 3].

Conditions of HPHT are of major concern because of the high demands of the materials involved, and the presence of seawater in the pipeline liquids makes corrosion a pervasive issue across the industry. In general, the extremity of the HPHT zone tends to accelerate the material degradation processes, forcing early and costly replacements. For this reason, process equipment, wells, tanks, and pipelines in the HPHT zones are often protected with high-performance epoxy-based anti-corrosive coatings. However, the durability and/or degradability of these highly cross-linked coating systems under the conditions of HPHT (including the presence of gases such as H_2S and CO_2, along with a mixture of hydrocarbon fluids and seawater [4-7]) are rarely reported in the open literature and the underlying mechanisms remain largely unexplored. Furthermore, Rapid Gas Decompression (RGD), i.e. when depressurization to ambient conditions takes place during emergency shutdowns, can also lead to failures (e.g. crack initiation and growth in cross-linked networks [8]) caused by the fast release of gases dissolved in the coating.

Due to superior mechanical strength and toughness, as well as outstanding chemical, moisture and corrosion resistance, epoxy-based coating systems are important candidates for mitigating corrosion issues for conditions of HPHT [9, 10-11]. However, studies from recent years have found that degradation mechanisms of resin systems under extreme HPHT conditions are still largely unresolved [8, 12-13]. While investigations on epoxy coatings related to each of the three HPHT phases individually (i.e. gas, hydrocarbon, and seawater) are abundant at or close to atmospheric pressure [14-29], no studies appear to have explored the presence and combined effects of all three phases at HPHT on coatings.

The effects of temperature on the oxidation and thermal degradation of epoxy networks were found to be significant [14-16]. A case study on high-temperature (110 ^{o}C) oxidation of epoxy coatings suggested that long-term aging of epoxy amine networks proceed via oxidative degradation that leads mainly to amide group formation at the vicinity of tertiary amines [14]. In other investigations [15, 16], the thermal oxidation kinetics of DGEBA epoxy systems (ranging from 70 to 150 ^{o}C) were found to result in gas evolution (e.g. H_2, CO, CO_2, CH_4), the formation of double bonds, carbonyl and amide groups, and chain scissions that leads to the decrease of its mechanical properties.

Studies on the effects of elevated pressures on epoxy coatings, on the other hand, are lacking even though an investigation points out that with increasing pressures, the solubility of gases in water increases, thereby intensifying their corrosive properties [17]. Using de-ionized water as the medium, Liu et al. [18] compared the performance of an epoxy coating system at atmospheric pressure and a hydrostatic pressure of 35 atm. They found that the pressure changed the electrochemical behaviour of the coating and induced a failure process that deteriorated the protective properties by accelerating the absorption and diffusion of water. This also changed the diffusion type from ideal to non-ideal Fickian with an S-shaped transient absorption behaviour. The investigations further showed that in the absence of liquid water, the coating may resist degradation under high pressure [18, 19]. Although HPHT definitions state a pressure rating of 690 bars, in the present study, HPHT also refers to the extreme conditions of temperature/pressure encountered by the metal substrate in the upstream oil and gas applications and various industries e.g. pipeline coatings and buried and submerged steel structures, namely storage tanks and coatings for drilling wells reinforcement [20]. Subsequently, a benchmark pressure of 130 bars and a temperature of 180 ^{o}C was maintained for all the experiments.

In the presence of CO_2, high-pressure conditions were reported to be even more detrimental to epoxy networks. Dong et al. [21] studied the degradation of epoxy coatings in the presence and absence of CO_2 at different temperatures. In the absence of CO_2 and when immersed in seawater, small blisters were observed in the coating, without any loss of coating adhesion to the substrate. However, in the presence of CO_2, blister formation was enhanced, and steel corrosion was observed under the film, ultimately leading to a complete loss of coating adhesion, which was attributed to higher diffusion rates of water into the coating network. Similarly, the presence of sulphur components (H_2S gas in particular) is well known for some HPHT conditions.

Solvent permeability and sorption studies of epoxy networks have shown that the T_g is sensitive to solvent ingress [22, 23], and it can probably be anticipated that this effect is intensified at HPHT conditions with crude oil containing a large amount of aromatic hydrocarbons (para-xylene being an important representative). Additionally, seawater, with its strong corrosive ability (attributed mainly to the chloride ion), plays an important role in the degradation pathways [24-27]. Similarly, application temperature, pH, dissolved gases, and mineral constituents in the water all influence the corrosion process [24, 27]. In essence, all three phases present at HPHT conditions can influence the rate and degree of epoxy coating degradation, and in particular, attention must be paid to the presence of CO_2, aromatic solvents, and seawater.

The present work has two aims. One is to understand the degradation behaviour of an amine-cured epoxy novolac (EN) and an amine-cured bisphenol F (BPF) epoxy coating under conditions of HPHT, the other to assess the interaction of the three HPHT phases with the two coatings. The formulations considered are epoxy-based coatings, consisting of a resin (base) and a curing agent only. Exclusion of pigments, fillers and additives allows a more accurate description and interpretation of the resin system degradation pathways. Furthermore, when developing a coating formulation, the resin system is the principal ingredient. The choice of either epoxy novolac or bisphenol F as the base and a polyamine as the curing agent was based on the high functionality, good bonding properties and excellent resistance to water and solvents of these cross-linked coating systems [28-33]. This study is the first step towards developing an efficient and high performing epoxy formulation, keeping in mind the wide variety of chemical reactions that can be used for the curing of epoxy resins. A knowledge of the epoxy cross-link chemistry may also allow for the control of the degree of cross-linking and thereby the physical and chemical coating properties required for HPHT conditions.

Along with applications in HPHT zones, the research and findings of the present study are of relevance for coating applications in e.g. drilling wells reinforcement techniques, heat exchanger tubes, incinerators for organic waste, high temperature-exposed parts in space applications and high-pressure engine combustion chambers [34-38]. Another worthy mention is the next generation carbon capture and storage (CCS) application, where the current research findings can support formulation of supercritical CO_2 ($SCCO_2$) resistant coatings for pipelines involving transport of $SCCO_2$ from power plants to geological sequestration sites [39].

2. Experimental

2.1. Coating materials and application

Using a DEN 438 epoxy novolac resin (functionality, f, of 3.6) as the base and a mixture of DEAPA adduct and MXDA adduct amine hardeners as curing agents, an epoxy novolac (EN) coating was formulated. Similarly, using EPON 862 (f = 2.1) as the base and Amicure PACM cycloaliphatic amine as the hardener, a Bisphenol F (BPF) coating was prepared. The molecular structures of the raw materials used to formulate the EN and BPF coatings are described in Table 1 and 2, respectively.

Table 1. Molecular structures of raw materials used for the EN coating.

Formulation 1 Raw Materials	**Epoxy Novolac (EN) coating (f = 3.6)**		
Base	**Molecular Structure**	**Epoxide equivalent weight [g/mol of epoxide]**	**Epoxide content [mmol/kg of epoxy resin]**
DEN 438 Novolac resin	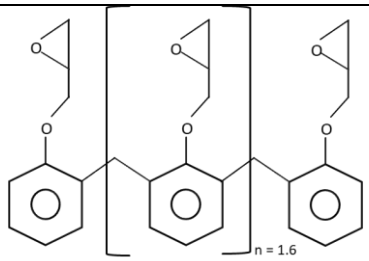	176 – 181	5525 - 5680
Curing agents	**Molecular structure**		
DEAPA Adduct – Curing agent 1	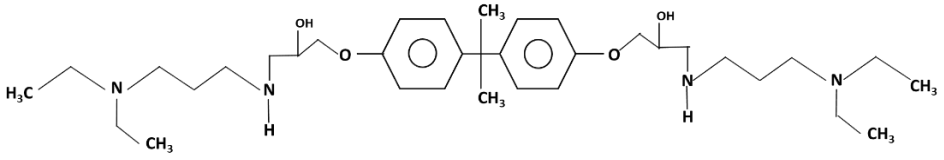		
MXDA Adduct – Curing agent 2	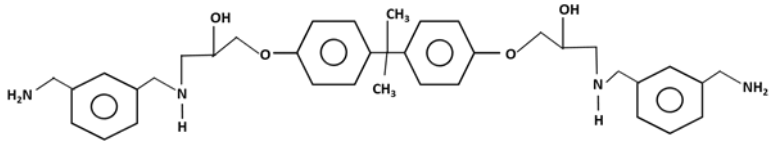		

Table 2: Molecular structures of raw materials used for the BPF coating.

Formulation 2	**Bisphenol F (BPF) coating (f = 2.1)**

Raw Materials			
Base	**Molecular Structure**	**Epoxide equivalent weight [g/mol of epoxide]**	**Epoxide content [mmol/kg of epoxy resin]**
EPON 862 Bisphenol F resin	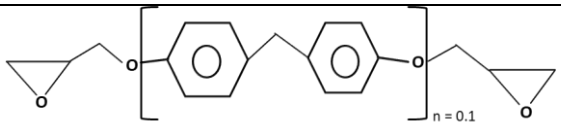	169	5938
Curing agent	**Molecular structure**		
Amicure PACM	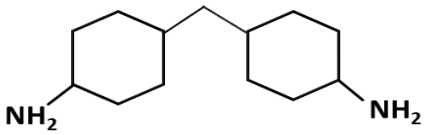		

The substrate used in the present study was mild steel with dimensions 5 mm x 70 mm x 120 mm, and the EN and BPF coatings were applied on both sides of the steel substrate, covering also the edges. Application of two coats, targeted each at 75 ± 15 µm dry film thickness (DFT), was done using a smooth natural bristle paintbrush of width 50 mm. A magnetic gauge instrument, Elcometer model 355 Top, was used to measure the total DFT (150 ± 25 µm). The recoating interval for the two coats (both EN and BPF) was 12 hours, and the coatings were allowed to cure for five days at room temperature. In the case of the EN, room temperature curing was followed by post-curing at 120 ^{o}C for 5 hours, and the stoichiometric ratio (from 0.3 to 0.6) between base and curing agent was selected to allow for the presence of free epoxy groups after room temperature curing. The elevated curing temperature then promotes further cross-linking among the free epoxy groups, which enhances the cross-linking density and thereby the physical and mechanical properties of the EN network. However, the lower functionality in the case of BPF restricts post-curing, because no surplus epoxide functional groups are available for further reaction. Moreover, for EN and BPF, the functional group stoichiometric ratio between the epoxy base and the curing agents, as well as the curing conditions, were selected to be in agreement with the commercial grade formulations available for HPHT applications.

2.2. HPHT coating reactor

To simulate HPHT conditions, the present study used a 4621 HPHT batch reactor model from Parr Instruments, equipped with a non-stirred chamber, capable of withstanding a temperature of 350 ^{o}C and a pressure of 180 bars. A schematic representation of the HPHT reactor setup with indication of phases and coated samples is shown in Fig. 1.

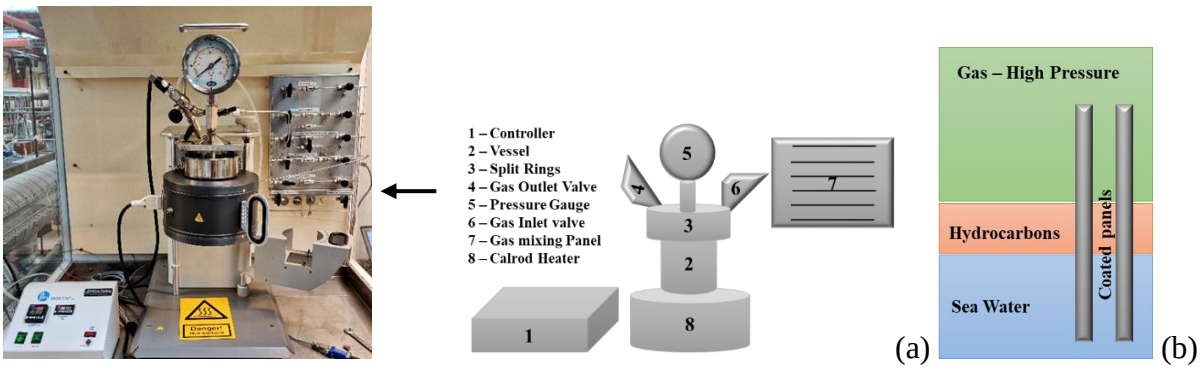

Fig. 1. (a) Schematic illustration (with photo) of the HPHT reactor and (b) coated panels inside the pressure chamber.

The reactor chamber (0.97 L) is made of Hastelloy C-276, a nickel-chromium-molybdenum alloy resistant to extremely corrosive environments. It is connected to multiple gas lines, a controller box, a calrod heater (i.e. a tubular heating element that converts electricity into radiant heat), a pressure gauge and safety valves. The gas lines allow N_2 and CO_2 gases to establish the required high pressures. Four coated panels at a time can be placed inside the chamber. In the present experiments, the gas-phase consisted of a mixture of N_2 and CO_2 at a pressure of 130 bars, maintained throughout the experiment. The hydrocarbon phase consisted of aromatic solvent (namely para-xylene), and a 3.5 wt.% NaCl solution made up the seawater phase. Although 3.5 wt.% NaCl represents the seawater phase in the present study, the complexity of the water phase at HPHT (commonly known as "produced water" [40]) varies depending on geologic age and depth. The produced water contains the same salts as seawater, with sodium and chloride as the most abundant ions, but most produced waters have salinities and densities greater than that of seawater [41]. The salt concentration (salinity) of produced water may range from a few weight per cent to that of a saturated brine (about 30 wt.%), compared to a salinity of 3.2–3.6 wt.% for seawater [40].

Upon closing the chamber, flushing out O_2 from inside the chamber was the first step, conducted with the purging of high-pressure N_2 gas for 20 minutes, after which a requisite mixture of N_2 and

CO_2 was pumped into the chamber to reach a pressure of 100 bars at room temperature. Using a calrod heater, this pressurized chamber was then heated to 180 ^oC at a heating rate of 5 ^oC/min, whereby the pressure increased to 130 bars. For all experiments, the pressure maintained was 130 bars at 180 ^oC for an exposure time of 12 hours.

The final step, before taking the exposed samples for analysis and characterization, was cooling to room temperature, followed by pressure release at a rate of 500 bars/min, simulating the real-life rapid shutdown procedure in HPHT wells. This last step is known as rapid gas decompression (RGD) in the HPHT domain.

2.3. Characterization techniques

2.3.1 Surface characterization techniques for analysis before and after HPHT exposure

The surface morphology of EN and BPF specimens before and after HPHT was analyzed with a scanning electron microscope (SEM) (Prisma E-SEM, manufacturer Thermofisher Scientific, Denmark), operated at an accelerating voltage of 20 kV, and a digital microscope (VHX-6000, manufacturer Keyence, Belgium) with the lens VH-Z20T, which can magnify up to 200 times. Energy-dispersive X-ray (EDX) analysis coupled with SEM was used to qualitatively identify the presence of any heterogeneities at the surface.

2.3.2 Attenuated total reflection-Fourier transform infrared spectroscopy (ATR-FTIR)

To investigate the degradation mechanisms of the EN and BPF coatings, an ATR-FTIR study was conducted before and after HPHT exposures. An IFS 48 ATR-FTIR instrument from Bruker (Ettlingen, Germany) was used to investigate the chemical changes in the cross-linked network. The absorbance mode was in the range of 400–4000 cm^{-1} and at a resolution of 4 cm^{-1}.

2.3.3 Differential scanning calorimetry (DSC)

Using a ‘Discovery’ Model DSC apparatus (manufacturer TA Instruments, Denmark), DSC studies were performed. To monitor the change in specific heat capacity of EN and BPF coatings before and after HPHT exposures, dynamic experiments were executed. A few milligrams of the EN or BPF coating were scraped off in flake form, before and after HPHT exposure, and placed in closed aluminum DSC pans, before spectra were recorded from room temperature to 350 °C at a 10 °C/min heating rate.

3. Results and Discussion

The results and findings, which now follow, originate from analysis of the surface characteristics of EN and BPF coatings and from examination of the changes in functional group concentrations of the cross-linked networks. Average T_g depressions of the coatings were also measured for each of the three HPHT exposure zones.

3.1 Optical analysis before and after the HPHT exposure

3.1.1 Visual inspection

HPHT exposure of the EN and BPF coatings led to three distinct surface zones resulting from each of the three HPHT phases, as shown in Fig. 2 and Fig. 3.

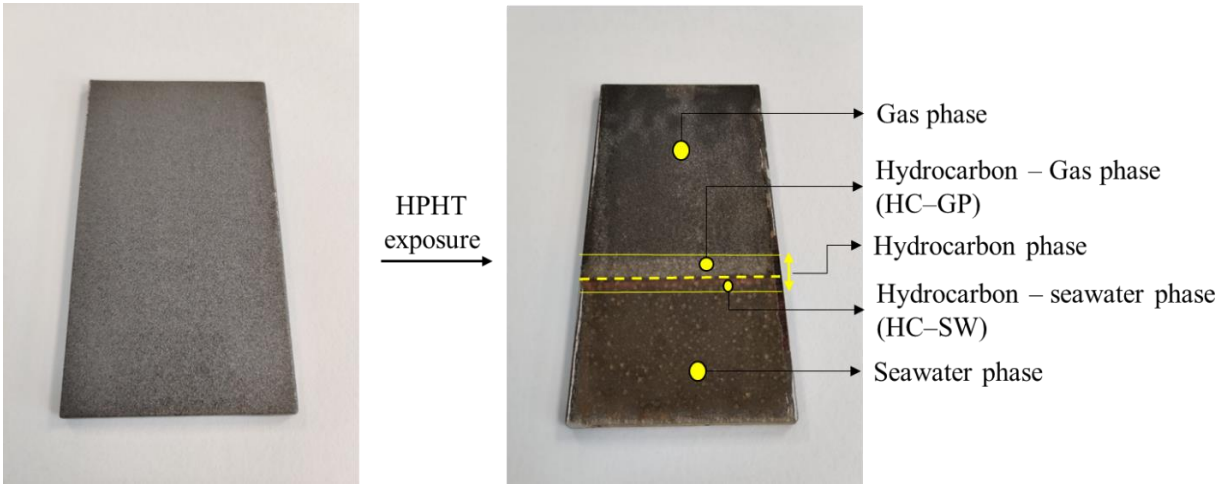

Fig. 2. Non-magnified photographs of the EN coating before and after the HPHT exposure, exhibiting three resultant zones and two sub-zones, namely HC–GP and HC–SW at the hydrocarbon-exposed zone.

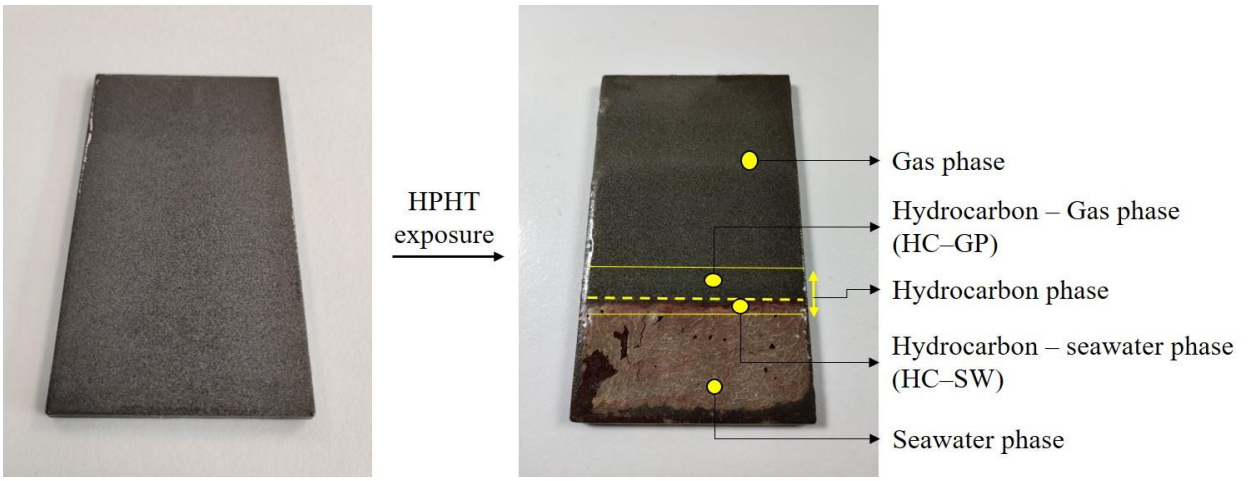

Fig. 3. Non-magnified photographs of the unexposed BPF coating (left) and after the HPHT exposure (right), displaying similar tendencies to degradation as those of EN.

The type of defects seen in the two coatings was similar, but the severity of the degradation was different. For the gas phase (i.e. N_2 and CO_2) exposed zone, there was no change in the surface appearance for either system. In the hydrocarbon (para-xylene) exposed area, on the other hand, both EN and BPF exhibited two subzones; one towards the gas phase, termed the HC–GP zone, showing a mild discolouration, and the other towards the seawater phase, designated as the HC–SW zone, where a characteristic red particulate layer was deposited. Lastly, at the seawater-exposed zone, formation of blisters was prominent for the EN network, while the BPF coating exhibited an almost complete loss of adhesion between the coating and the steel substrate.

3.1.2 Digital Microscopy

The digital microscope provides a high depth of field and in Fig. 4 and Fig. 5, micrographs for the resultant zones on the coating surfaces are shown. In the case of EN, the gas phase-exposed zone (Fig. 4a) showed no sign of degradation, disregarding some micropores and surface defects also present in the virgin coating, which are often seen for coatings without additives. In the hydrocarbon-exposed zone, a number of minute pinholes were spotted at the HC–GP zone (Fig. 4b). In the HC–SW zone (Fig. 4c), close to the seawater interface, a dark red-coloured layer with a grainy structure was deposited on the surface covering the pinholes, and the seawater-exposed zone (Fig. 4d) was scattered uniformly with voids and micropores.

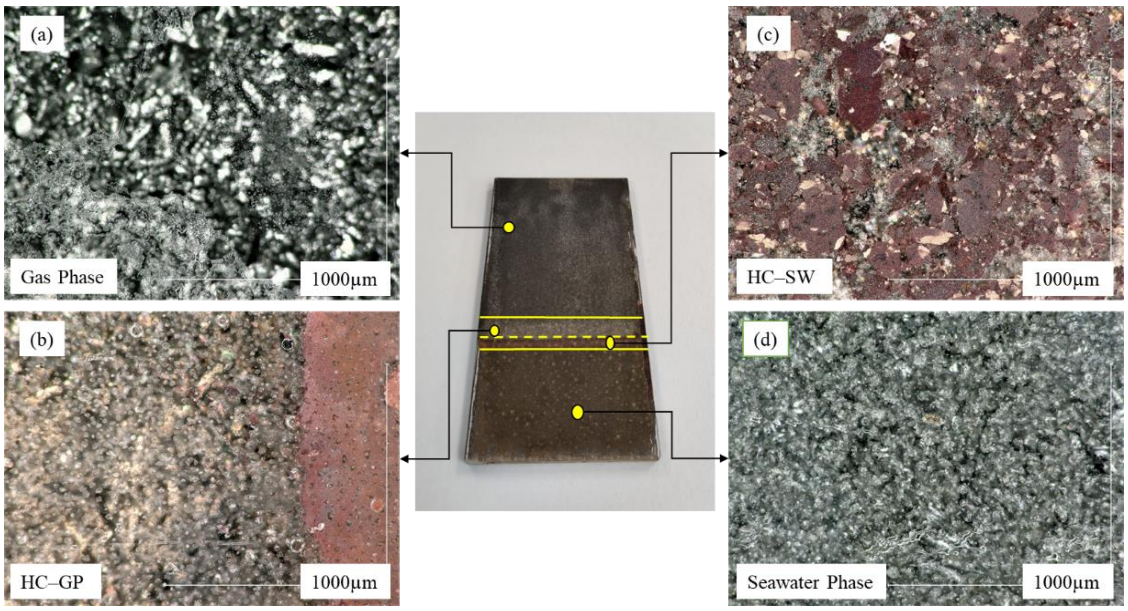

Fig. 4. Optical micrographs of EN surface defects at (a) gas-exposed zone, (b) the HC-GP zone, (c) the HC-SW zone, and (d) seawater-exposed zone after HPHT exposure.

For the BPF network, surface defects similar to those of EN can be observed for the gas phase (Fig. 5a) and the HC–SW zone (Fig. 5c), except for a reduced number of pores in the HC–GP zone (Fig. 5b). In the seawater-exposed zone (Fig. 5d), compared to EN, BPF shows cracks, fissures, larger pores and an almost complete loss of adhesion between the coating and the substrate.

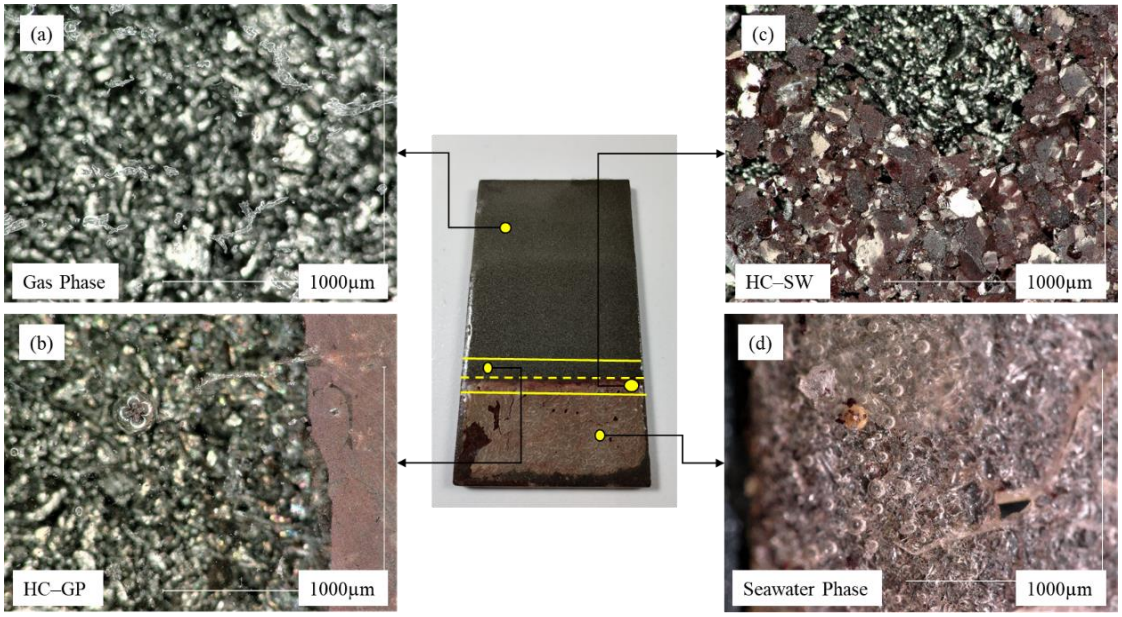

Fig. 5. Optical micrographs of the resultant zones, showing surface defects on the BPF coating after HPHT exposure.

To confirm the composition of the red-coloured grainy structure formed on the hydrocarbon-exposed zone of both EN and BPF, elemental mapping using the SEM-EDX characterisation was performed. Using this method, the heterogeneity of the seawater-exposed zone was also examined.

3.1.3. SEM – EDX analyses

To substantiate the defects and changes developed at the coating surface, SEM micrographs of the EN and BPF coatings were used. Fig. 6a and 6b show the surface morphology of unexposed EN and BPF coating respectively and, since the formulations are without additional solvents and film forming agents, minor, unproblematic, surface imperfections are present. The gas phase-exposed zones of EN (Fig. 6c) and BPF (Fig. 6d) after exposure showed similar surface imperfections implying no significant interaction with the HPHT gas phase.

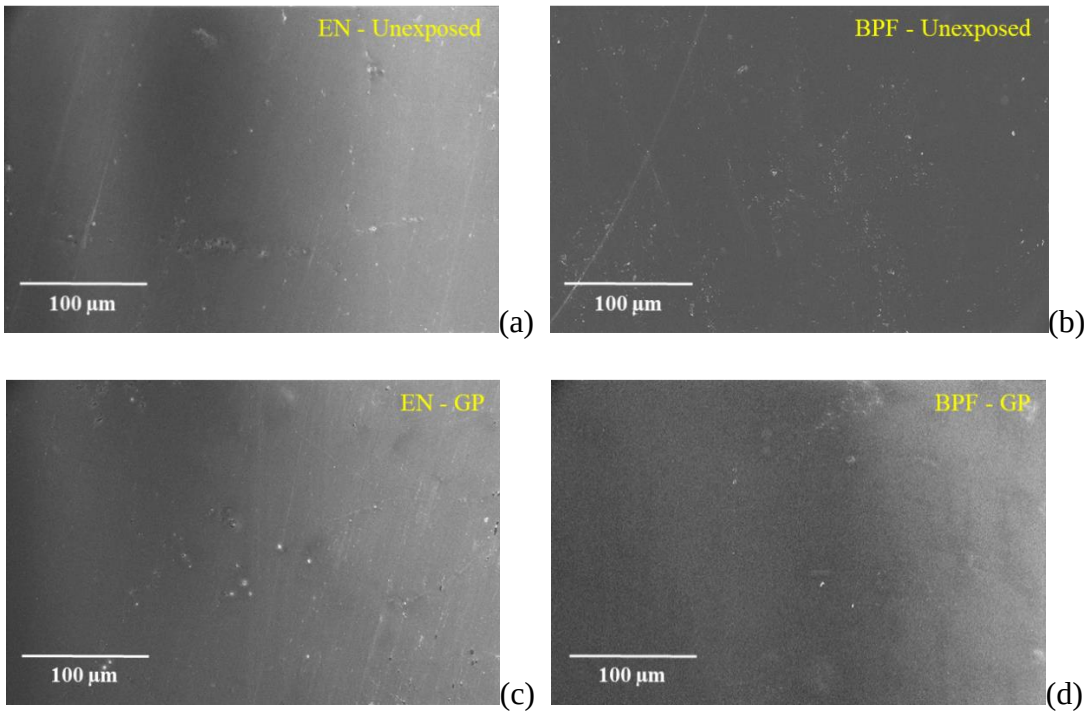

Fig. 6. SEM micrograph of the unexposed (a) EN and (b) BPF coating and the gas phase-exposed area of (c) EN and (d) BPF coating after HPHT exposure.

The HC–GP zone for EN suffers from a darkened surface, as well as numerous craters of a size from 15 to 30 µm. In the HC–SW zone, in addition to voids, deposition of a discrete structural

layer is evident as specified by the yellow marker in Fig. 7a. Contrarily, for the HC–GP zone of the BPF network (Fig. 7b), the coating surface remained intact and was free of any major defects. However, severe degradation in the form of a layer deposition at the HC–SW zone, similar to that of the BPF, was observed. This layer conforms to the red-coloured grains with well-defined structures mentioned earlier.

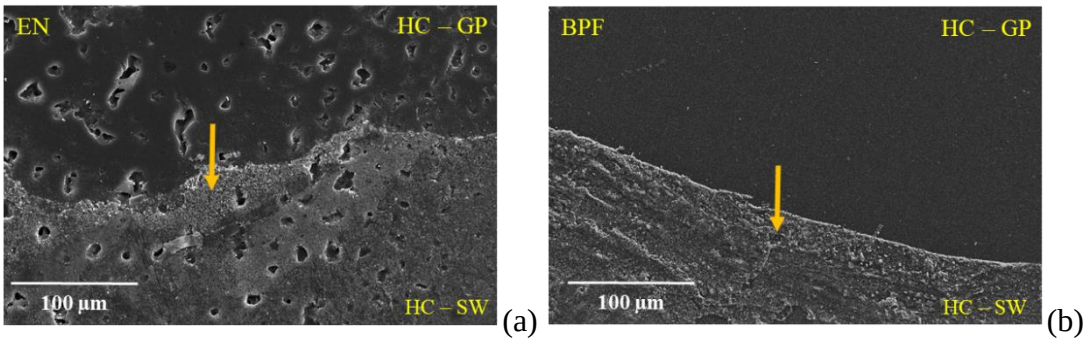

Figure 7. SEM micrograph of the hydrocarbon zone showing the two zones (HC–GP) and (HC–SW) for both EN (a) and BPF (b).

An elemental analysis, using EDX mapping at the HC–SW subzone for EN (Fig. 8) and BPF (Fig. 9), confirmed the red-coloured deposit to be an oxide of iron. Under the present experimental conditions, the only iron source is the steel substrate, which implies that seawater and CO_2 in the HC–SW subzone finds access to the steel-coating interface, where it permits anodic reactions of iron to form Fe^{2+} (ferrous) ions. The latter diffuse to the coating surface where they precipitate as oxides in the HC–SW subzone. Later, in section 5.4, the mechanism for the underfilm corrosion at the HC–SW subzone, and its absence in the gas and seawater-exposed zone, is explored.

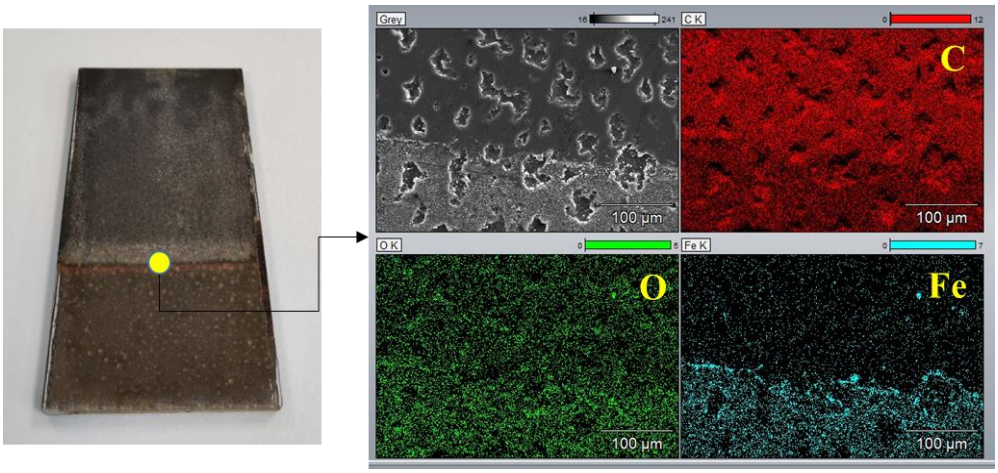

Fig. 8. Elemental (EDX) mapping of Fe (and C and O) for the EN coating, confirming the presence of an iron oxide in the HC-SW zone.

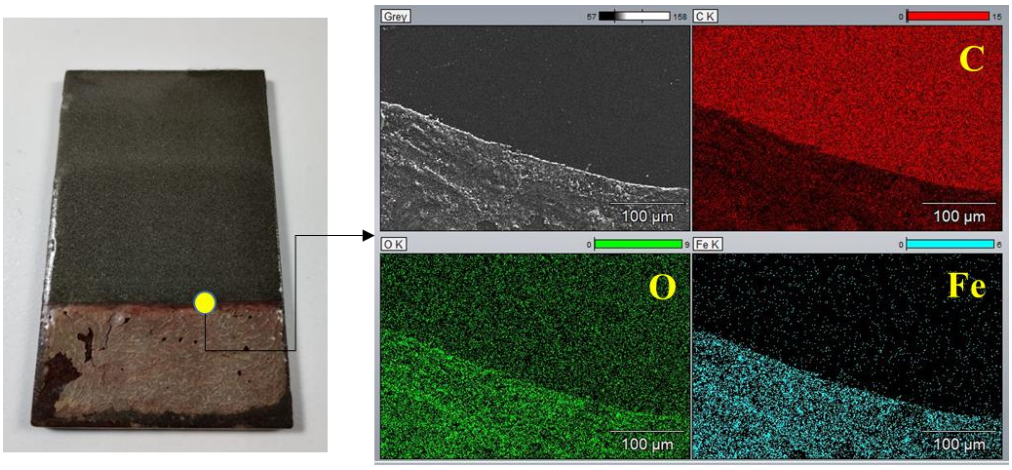

Fig. 9. Elemental (EDX) mapping confirming iron oxide at the HC–SW zone of the BPF coating.

The SEM micrographs in Fig. 10a and 10b show the topography for the seawater-exposed zone of the EN and BPF coatings, respectively. The EN micrograph demonstrates a significant number of voids in combination with pinholes (marked with red circles) as characteristic defects all over the seawater-exposed surfaces, whereas the SEM micrograph of BPF show cracks and crevices (marked with yellow circles) at the exposed surface, along with completely chipped-off structures signifying severe seawater permeation through the network.

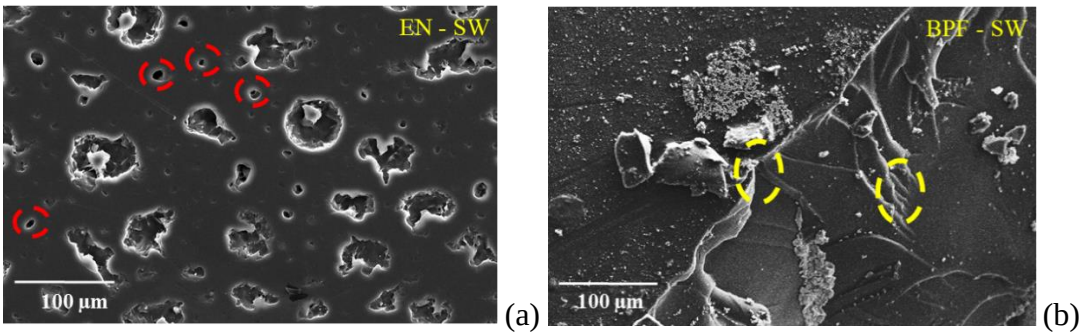

(a) (b)

Fig. 10. A SEM micrograph of the seawater-exposed area for (a) EN and (b) BPF coating.

The elemental mapping performed for the seawater-exposed zone of both EN and BPF is shown in Fig. 11 and 12, respectively. The EN showed greater resistance to seawater diffusion with micro pinholes as the major type of defect, along with trace amounts of chloride ions deposited at the

surface. In the case of BPF, the chloride ions were observed in between the crevices, confirming ion permeation into the bulk of the coatings, resulting in higher water uptake. This is in good agreement with a previous study [32], which confirmed diffusion of seawater to the steel-coating interface with an almost complete loss of adhesion.

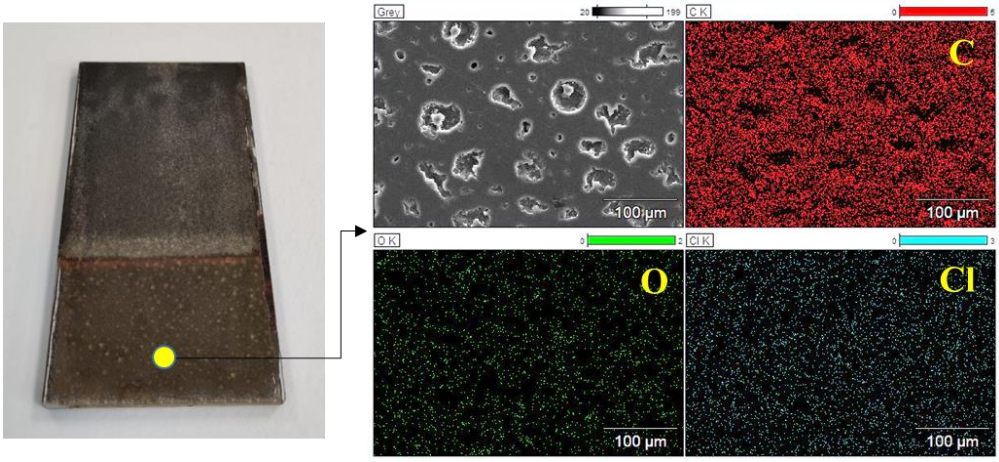

Fig. 11. EDX analysis, displaying chloride ions deposited uniformly on the SW zone for EN.

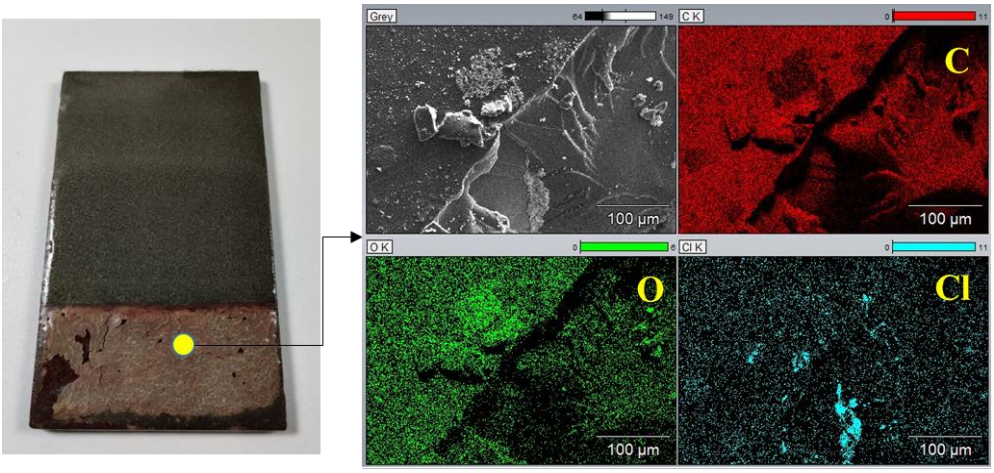

Fig. 12. EDX analysis confirming aggregates of chloride ions for the SW zone of BPF.

The SEM-EDX investigations suggest that the physical coating degradations under conditions of HPHT occur through the formation of voids, pores and pinholes, and through loss of adhesion.

3.3. ATR-FTIR analysis

To understand the chemical interaction of the EN and BPF cross-linked networks with the HPHT phases, ATR-FTIR analysis was performed on each of the three HPHT exposure zones. The FTIR

spectra of EN and BPF are shown in Fig. 13 and 14. FTIR spectra for each zone (both EN and BPF samples) were measured in three different areas to account for the repeatability.

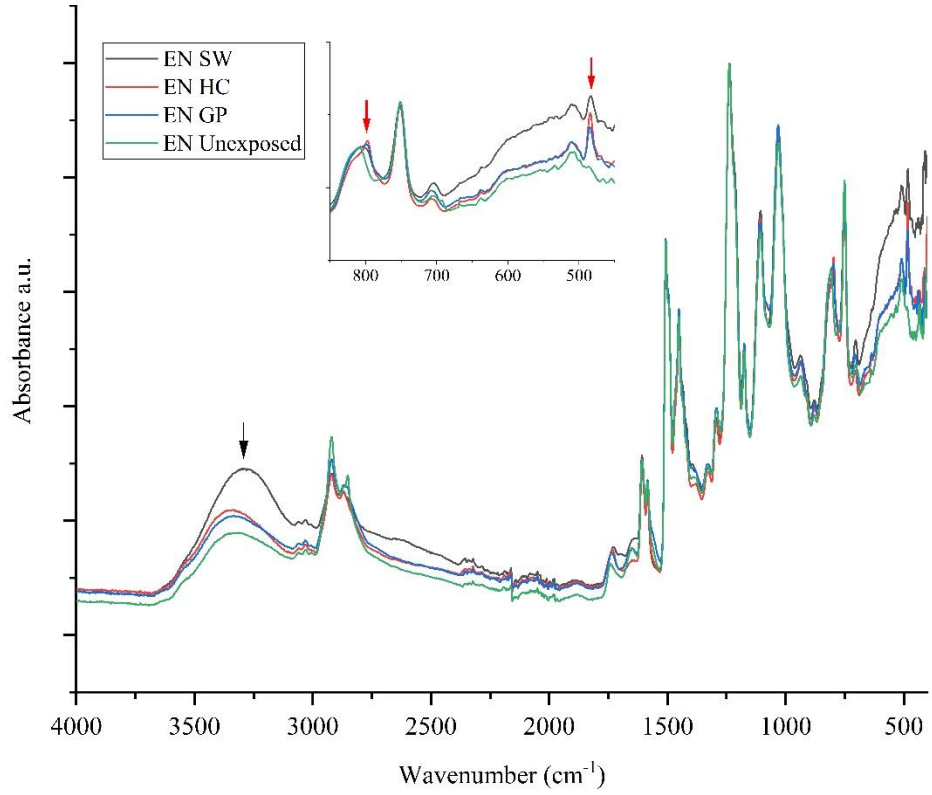

Fig. 13. FTIR absorption spectra of the EN coating before and after HPHT exposure.

The spectra of EN and BPF cross-linked networks both show a stretching vibration of N–H and O–H bonds in the range from 3,800 to 3,200 cm^{-1}. The stretching of the CH_2 and CH_3 groups were visible just below 3,000 cm^{-1}. The 1507 and 1605 cm^{-1} correspond to absorption by C=C groups of the benzene rings. Absorptions at 1230 cm^{-1} were caused by the stretching vibration of the in-plane deformation of C-O of phenolic groups. The medium and broad absorption band at 1033 cm^{-1} was assigned to stretching vibrations of the aliphatic C-O functional groups. The strong peak at 810 cm^{-1}, on the other hand, was attributed to the C-H bending vibration of the aromatic ring in the novolac cross-linked network. As a result of the post-curing step, the carbonyl peak at 1660 cm^{-1} was observed in the unexposed EN sample (Fig. 13). The same appears for all the zones of EN after HPHT exposure. Due to the presence of unreacted epoxy functional groups in the case of

the unexposed BPF sample, a small peak at 910 cm^{-1} was seen. To avoid any excess of amine curing agent, eliminating the chances of amine blushing, the stoichiometric ratio for BPF was purposely selected to 5 to 7 wt.% less than full cure.

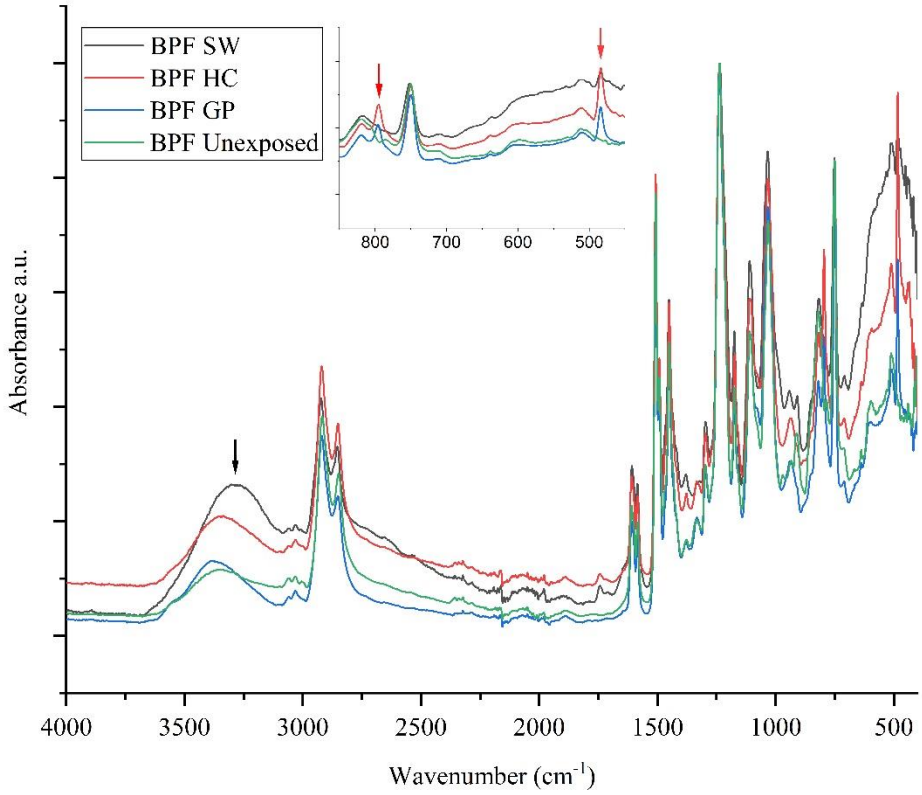

Fig. 14. FTIR spectra of BPF coating before and after HPHT exposure.

Following the HPHT exposure, the FTIR spectra of EN and BPF showed no significant change in any of the three exposed zones, except for an increase in the peak located at 3200–3800 cm^{-1} (marked by a black arrow in the insert pictures) associated with a hydroxyl group (-OH) in the seawater-exposed zone. This peak increase in the seawater-exposed zone for both EN and BPF was directly associated with the diffusion of seawater through the cross-linked network [42]. Additionally, the RGD in the present study would enable some of the entrapped water molecules to migrate to the coating surface, resulting in an increased hydroxyl peak at the seawater-exposed zone. Furthermore, the peaks at 795 and 485 cm^{-1} (marked by red arrows in the insert pictures)

precisely larger for the HC zone after HPHT exposure, associated with the out-of-plane bending of –CH groups of the substituted benzene (aromatics), were evidence of para-xylene ingress into the EN and BPF coating network after HPHT exposure. Except for the hydroxyl group peak and the substituted benzene peaks, there was no appreciable change observed in the spectra for any of the three exposed zones, confirming the absence of any additional chemical reactions or changes in the functional groups. This suggests that physical degradation is dominant over chemical degradation under conditions of HPHT. To test if the intact BPF and EN coatings were partially soluble in the para-xylene or if any degradation or chain scissions could be detected, the hydrocarbon liquid (para-xylene) after HPHT exposure was examined using Liquid Gas Chromatography (LGC) and compared to the hydrocarbon liquid before HPHT exposure. However, the LGC results showed no functional groups in the exposed hydrocarbon liquid, confirming the absence of any solubility or scissions of either EN or BPF coatings at HPHT.

3.4. Differential scanning calorimetry (DSC) Analysis

The effect of HPHT conditions on the coatings as a function of change in the average T_g was measured using DSC analysis and the results for the three exposure zones are summarized in Table 3.

Table 3: Average glass transition temperatures (T_g) measured for the EN and BPF coatings before and after HPHT exposure. (DSC measurements were conducted at two different areas of each zone for both EN and BPF coatings.)

	Average T_g values in ^oC	
	EN	BPF
Before HPHT exposure (Unexposed)	155±3	133±2
Gas-exposed zone (GP)	152±4	131±3
HC–GP zone	135±2	105±3
Seawater-exposed zone (SW)	137±3	103±2

The T_g for EN before HPHT exposure was measured to 155±3 ^oC, and in the case of BPF, it was 133±2 ^oC. After HPHT exposure, T_g for both EN and BPF in the gas phase-exposed zone remained close to the initial values with 152±4 ^oC and 131±3 ^oC, respectively. The negligible difference in T_g depression at the gas phase-exposed zone means that high-pressure N_2 and CO_2 individually have no substantial effect on either of the coating networks. This resistance to CO_2 plasticization effects, namely swelling and blister formation, was attributed to the semi-crystallinity of epoxy

networks, owing to its 3D cross-linking, as opposed to purely amorphous networks [43]. Besides, for gas diffusion into epoxy networks, it was reported that it becomes a necessity for chain motions to be present [44]. The T_g measurements complemented the SEM micrographs, pointing out no major surface defects in the gas phase-exposed zone. Further validation of no thermal or chemical degradations of EN and BPF at the gas phase-exposed zone by FTIR analysis confirmed that CO_2 alone does not affect the EN and BPF networks under conditions of HPHT.

The most diverse change in the T_g values for EN and BPF was observed at the hydrocarbon-exposed zone. At the HC–GP zone of EN, the mild discoloration and voids observed with SEM and the T_g value depression of 20±2 ^oC, are evidence for the diffusion of para-xylene into the EN networks. At the HC–GP zone of the BPF network, the T_g was similarly found to decrease by 27±3 ^oC. This depression in the T_g values is evidence that the diffusion of para-xylene caused an increased chain motion (free volume increase) at the HC–GP zone of EN and BPF during HPHT. Para-xylene diffusion and the resultant T_g depression at the HC–GP zone, for both EN and BPF networks, show that the aromaticity of hydrocarbons tends to play a characteristic role, bringing about an increased chain motion of the epoxy cross-link network under HPHT conditions [44]. The increased chain mobility in EN and BPF networks, due to the para-xylene uptake, results from the para-xylene's cohesive energy density, which is similar to that of the epoxy cross-linked network. In addition, a similar dipole interaction and greater intermolecular attractions originate from the large surface area of para-xylene and the presence of aromatic groups in epoxy [45].

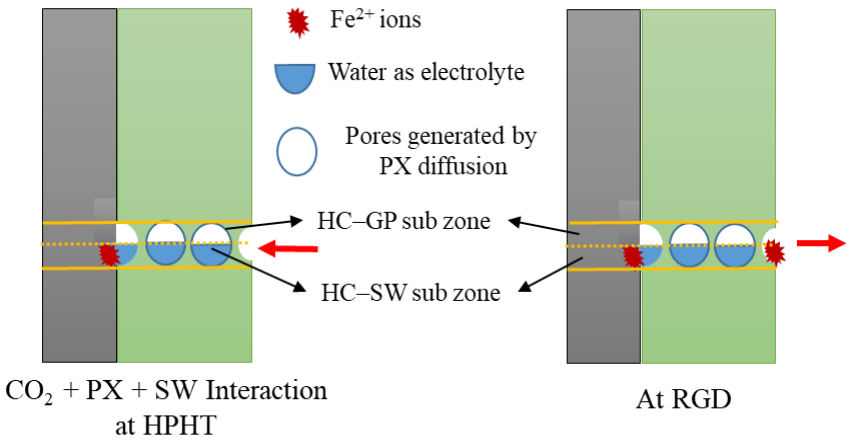

Fig. 15: Pathway for diffusion of ferrous ion to the coating surface during RGD at the HC–SW zone of EN and BPF networks. In the figure, PX is short for para-xylene.

Once the chain motion due to para-xylene interactions is increased at the hydrocarbon-exposed zone, the underlying steel substrate at the HC–SW zone is at high risk of being exposed to seawater. Additionally, CO_2 with its acidic properties, allows the seawater phase to permeate through the softened network reaching the steel coating interface. Note that the HC–SW subzone is the only zone where all three components, CO_2, para-xylene and seawater, act synergistically. Due to a ready access of electrolyte-containing water and CO_2, this leads to an acidic environment due to formation of H_2CO_3 (carbonic acid) at high temperature [46] and a rapid corrosion of the underlying substrate at the steel-coating interface of the HC–SW zone. Anodic pitting of iron resulted in formation of ferrous ions (Fe^{2+}) releasing electrons, and the main cathodic reactions were the hydrogen evolution from H^+, H_2CO_3 and H_2O [47]. Due to para-xylene uptake initially, the resultant free volume increase and the subsequent seawater permeation to the steel-coating interface formed the pathway for the characteristic underfilm corrosion at the HC–SW zone of both EN and BPF. The final step of RGD, where the built-up pressure is released at a rapid rate (decompression), also aided the Fe^{2+} and the underfilm corrosion products formed to precipitate precisely at the HC–SW zone, depositing oxides of iron for both EN and BPF networks (see Fig. 15).

Seawater uptake for EN and BPF networks at HPHT followed a trend showing the dependency of water permeation on the synergistic action of temperature, pressure and CO_2, and the T_g measured for the EN coating at the seawater-exposed phase was 137±3 ^oC. However, the absence of increased chain motion at the seawater-exposed zone limited the direct penetration of seawater to the steel-coating interface, unlike the case of the softened HC–SW zone for EN. Due to water permeation, the defects in this case were mainly physical, in the form of blisters and macro pinholes at the coating surface. The presence of CO_2 in HPHT conditions increased the overall acidity of the seawater, thereby increasing the corrosion rate [47]. Besides, the high-pressure condition constantly acted as a driving force for the seawater to penetrate the EN and BPF networks, exerting a greater force than the coating cohesion, thereby giving rise to the formation of minor blisters [48]. The fact that the exposure temperature was substantially higher than the T_g of the EN network, was a more important contribution to the rate of water penetration than the high-pressure effect on the free volume. Hence, the high temperature maintained at HPHT plays an important role, even under compressed coating network conditions, allowing faster water penetration. Furthermore, our preliminary study [49] confirmed no direct effect of a slow pressure

release on the extent of coating degradation. The pressure of 130 bars maintained in the present study is so high that a slow depressurization (as slow as 1 bar/min), as opposed to 500 bars/min, also resulted in the formation of blisters, similar in size and quantity. Therefore, the high pressure conditions and the rapid gas release (RGD) are a relatively more prominent origin for the blisters in the HPHT seawater zone than the common osmotic or cathodic blistering. However, the EN network behaved as an impermeable membrane, restricting ions and water molecules to penetrate to a lesser extent at the seawater-exposed zone, sustaining a good adhesion to the substrate.

In the case of BPF, the degradation was more severe than for EN, as water molecules, along with chloride ions were confirmed by EDX analysis (Fig. 12) to penetrate the entire coating thickness reaching the steel-coating interface. This resulted in an almost complete loss of adhesion at the seawater-exposed zone, where the T_g measured for BPF network was 110±2 ^oC. The lower functionality of BPF when compared to EN thus proved detrimental at the seawater-exposed zone and did not offer any resistance under HPHT conditions. The water uptake resulting in blister formation in the case of EN and an almost complete loss of adhesion for BPF network followed the traditional volumetric and interactional approach [29, 50]. Here, the volumetric approach was associated with the permeation of seawater through the macromolecular chains present in the epoxy network under the effect of high pressure [51, 52]. The interactional approach, on the other hand, was attributed to the diffusion of water molecules into the cross-linked network via hydrogen bonding with polar groups, mainly the hydroxyl and amine group in the cured epoxy network [53, 54].

4. Conclusions

To study, under simulated high pressure and high temperature (HPHT) conditions, the degradation pathways for EN and BPF amine-cured anticorrosive coatings, a closed reactor (autoclave) was used. When exposed to HPHT, the EN and BPF coatings revealed three degradation zones. The gas-phase-exposed zone remained unaffected for EN and BPF networks, which means that high-pressure N_2 and CO_2 gases by themselves do not affect the epoxy networks under HPHT conditions. Para-xylene interactions, on the contrary, at HPHT led to increased chain motion in both EN and BPF networks, thereby lowering the coating glass transition temperatures significantly. The free volume increase served as the initiation point for the CO_2 and seawater

permeation into the EN and BPF networks and as a result, anodically-dissolved iron from the steel-coating interface solidified as iron oxides at the HC–SW exposed surface.

Minimal, yet sufficient water uptake, generating blisters and macro pinholes in the case of EN, was observed in the seawater-exposed zone. On the other hand, water molecules permeated to the steel-coating interface in the BPF network, resulting in an almost complete loss of adhesion under HPHT conditions.

The selection of the resin system is one of the most important parameters in designing a coating formulation, and it can be concluded that the formulated EN coating performs superiorly to BPF at HPHT.

Acknowledgements

Financial support from the Hempel Foundation to CoaST (The Hempel Foundation Coatings Science & Technology Centre) is gratefully acknowledged. The authors would also like to thank Lars Thorslund Pedersen, Hempel A/S, for inspiring and helpful discussions on HPHT over the years.

Declaration of interest

None

References

1. Shadravan, A., & Amani, M. (2012, January). HPHT 101: What every engineer or geoscientist should know about high pressure high temperature wells. In SPE Kuwait International Petroleum Conference and Exhibition. Society of Petroleum Engineers.
2. Skeels, H. B. (2014, May). API 17TR8-HPHT design guideline for subsea equipment. In Offshore Technology Conference. Offshore Technology Conference.
3. Shell Appomattox, Gulf of Mexico's first HPHT program, receives BSEE approval. (2019, July 30). Retrieved January 21, 2020, from https://www.worldoil.com/news/2019/7/30/shell-appomattox-gulf-of-mexico-s-first-hpht-program-receives-bsee-approval.
4. Singh, A., Lin, Y., Ebenso, E. E., Liu, W., & Huang, B. (2014). Determination of corrosion inhibition efficiency using HPHT autoclave by Gingko biloba on carbon steels in 3.5% NaCl solution saturated with CO2. Int. J. Electrochem. Sci, 9, 5993-6005.

5. Elgaddafi, R., Ahmed, R., Hassani, S., Shah, S., & Osisanya, S. O. (2016). Corrosion of C110 carbon steel in high-pressure aqueous environment with mixed hydrocarbon and CO2 gas. Journal of Petroleum Science and Engineering, 146, 777-787.
6. Pu, F., Philip, R. P., Zhenxi, L., & Guangguo, Y. (1990). Geochemical characteristics of aromatic hydrocarbons of crude oils and source rocks from different sedimentary environments. Organic Geochemistry, 16(1-3), 427-435.
7. Kashefi, K., Chapoy, A., Bell, K., & Tohidi, B. (2013). Viscosity of binary and multicomponent hydrocarbon fluids at high pressure and high temperature conditions: Measurements and predictions. Journal of Petroleum Science and Engineering, 112, 153-160.
8. Schrittesser, B., Pinter, G., Schwarz, T., Kadar, Z., & Nagy, T. (2016). Rapid Gas Decompression Performance of elastomers–A study of influencing testing parameters. Procedia Structural Integrity, 2, 1746-1754.
9. Pham, H. Q., & Marks, M. J. (2000). Epoxy resins. Ullmann's Encyclopedia of Industrial Chemistry.
10. Jin, F. L., Li, X., & Park, S. J. (2015). Synthesis and application of epoxy resins: A review. Journal of Industrial and Engineering Chemistry, 29, 1-11.
11. Bello, S. A., Agunsoye, J. O., Hassan, S. B., Zebase Kana, M. G., & Raheem, I. A. (2015). Epoxy Resin Based Composites, Mechanical and Tribological Properties: A Review. Tribology in Industry, 37(4).Advincula, R. C. (2019, May).
12. Advincula, R. C. (2019, May). Superhydrophobic and Nanostructured HPHT Stable Polybenzoxazine Nanocomposite Coatings for Oil and Gas. In CORROSION 2019. NACE International.
13. Johnson, L. M., Ledet, E., Huffman, N. D., Swarner, S. L., Shepherd, S. D., Durham, P. G., & Rothrock, G. D. (2015). Controlled degradation of disulfide-based epoxy thermosets for extreme environments. Polymer, 64, 84-92.
14. Bellenger, V., & Verdu, J. (1985). Oxidative skeleton breaking in epoxy–amine networks. Journal of applied polymer science, 30(1), 363-374.
15. Zahra, Y., Djouani, F., Fayolle, B., Kuntz, M., & Verdu, J. (2014). Thermo-oxidative aging of epoxy coating systems. Progress in Organic Coatings, 77(2), 380-387.

16. Pei, Y. M., Wang, K., Zhan, M. S., Xu, W., & Ding, X. J. (2011). Thermal-oxidative aging of DGEBA/EPN/LMPA epoxy system: Chemical structure and thermal–mechanical properties. Polymer degradation and Stability, 96(7), 1179-1186.
17. Jähne, B., Heinz, G., & Dietrich, W. (1987). Measurement of the diffusion coefficients of sparingly soluble gases in water. Journal of Geophysical Research: Oceans, 92(C10), 10767-10776.
18. Liu, Y., Wang, J., Liu, L., Li, Y., & Wang, F. (2013). Study of the failure mechanism of an epoxy coating system under high hydrostatic pressure. Corrosion Science, 74, 59-70.
19. Jie, L., Xiang-Bo, L., Jia, W., Tian-Yuan, L., & Xiao-Ming, W. (2013). Studies of impedance models and water transport behaviours of epoxy coating at hydrostatic pressure of seawater. Progress in Organic Coatings, 76(7-8), 1075-1081.
20. Bahadori, A. (2015). Essentials of Coating, Painting, and Lining for the Oil, Gas and Petrochemical Industries. Gulf Professional Publishing.
21. Dong, Y., & Yu, D. (2009). Effect of CO_2 on property of anti-corrosion of epoxy coating. In ICPTT 2009: Advances and Experiences with Pipelines and Trenchless Technology for Water, Sewer, Gas, and Oil Applications (pp. 1561-1567).
22. Kaplan, M. L. (1991). Solvent penetration in cured epoxy networks. Polymer Engineering & Science, 31(10), 689-698.
23. Luo, Y. S., Wang, C. Y., Cheng, K. C., Chuang, T. H., & Guo, W. (2011). Permeabilities of solvents through epoxy membranes prepared via chemically induced phase separation. Desalination and Water Treatment, 34(1-3), 272-276.
24. Sørensen, P. A., Kiil, S., Dam-Johansen, K., & Weinell, C. E. (2009). Anticorrosive coatings: a review. Journal of Coatings Technology and Research, 6(2), 135-176.
25. Sabra, A., Lam, T. M., Pascault, J. P., Grenier-Loustalot, M. F., & Grenier, P. (1987). Characterization and behaviour of epoxy-based diaminodiphenylsulphone networks. Polymer, 28(6), 1030-1036.
26. Bellenger, V., Verdu, J., & Morel, E. (1989). Structure-properties relationships for densely cross-linked epoxide-amine systems based on epoxide or amine mixtures. Journal of materials science, 24(1), 63-68.
27. Morsch, S., Lyon, S., Smith, S. D., & Gibbon, S. R. (2015). Mapping water uptake in an epoxy-phenolic coating. Progress in Organic Coatings, 86, 173-180.

28. Banks, L., & Ellis, B. (1982). The glass transition temperatures of highly crosslinked networks: Cured epoxy resins. Polymer, 23(10), 1466-1472.
29. Laza, J. M., Julian, C. A., Larrauri, E., Rodriguez, M., & Leon, L. M. (1999). Thermal scanning rheometer analysis of curing kinetic of an epoxy resin: 2. An amine as curing agent. Polymer, 40(1), 35-45.
30. Palmese, G. R., & McCullough, R. L. (1992). Effect of epoxy–amine stoichiometry on cured resin material properties. Journal of Applied Polymer Science, 46(10), 1863-1873.
31. Ashcroft, W. R. (1993). Curing agents for epoxy resins. In Chemistry and technology of epoxy resins (pp. 37-71). Springer, Dordrecht.
32. Pham, H. Q., & Marks, M. J. (2000). Epoxy resins. Ullmann's Encyclopedia of Industrial Chemistry.
33. Pradhan, S., Pandey, P., Mohanty, S., & Nayak, S. K. (2016). Insight on the chemistry of epoxy and its curing for coating applications: A detailed investigation and future perspectives. Polymer-Plastics Technology and Engineering, 55(8), 862-877.
34. Cestari, A. R., Vieira, E. F., Silva, E. C., Alves, F. J., & Andrade Jr, M. A. (2013). Synthesis, characterization and hydration analysis of a novel epoxy/superplasticizer oilwell cement slurry–Some mechanistic features by solution microcalorimetry. Journal of Colloid and interface Science, 392, 359-368.
35. Fedrizzi, L., Andreatta, F., Paussa, L., Deflorian, F., & Maschio, S. (2008). Heat exchangers corrosion protection by using organic coatings. Progress in Organic Coatings, 63(3), 299-306.
36. Chen, K. S., Yeh, R. Z., & Wu, C. H. (1997). Kinetics of thermal decomposition of epoxy resin in nitrogen-oxygen atmosphere. Journal of Environmental Engineering, 123(10), 1041-1046.
37. Dursch, H. W., & Hendricks, C. L. (1987). Protective coatings for composite tubes in space applications.
38. KR, V. K., & Sundareswaran, V. (2011). The Effect of thermal barrier coatings on diesel engine performance of PZT loaded cyanate modified epoxy coated combustion chamber. JJMIE, 5(5).

39. Barrie, J., Brown, K., Hatcher, P. R., & Schellhase, H. U. (2005). Carbon dioxide pipelines: A preliminary review of design and risks. In Greenhouse Gas Control Technologies 7 (pp. 315-320). Elsevier Science Ltd.
40. Neff, J., Lee, K., & DeBlois, E. M. (2011). Produced water: overview of composition, fates, and effects. Produced water, 3-54, Springer.
41. Collins A.G (1975) Geochemistry of oilfield waters. Elsevier, New York, 496 pp.
42. Liu, M., Wu, P., Ding, Y., Chen, G., & Li, S. (2002). Two-dimensional (2D) ATR− FTIR spectroscopic study on water diffusion in cured epoxy resins. Macromolecules, 35(14), 5500-5507.
43. Damian, C., Escoubes, M., & Espuche, E. (2001). Gas and water transport properties of epoxy–amine networks: Influence of crosslink density. Journal of applied polymer science, 80(11), 2058-2066.
44. Burke, J. (1984). Solubility parameters: theory and application.
45. Blanks, R. F., & Prausnitz, J. M. (1964). Thermodynamics of polymer solubility in polar and nonpolar systems. Industrial & Engineering Chemistry Fundamentals, 3(1), 1-8.
46. Tanupabrungsun, T., Brown, B., & Nesic, S. (2013). Effect of pH on CO2 corrosion of mild steel at elevated temperatures. Proceedings of the CORROSION, 2348.
47. Anselmo, N., May, J. E., Mariano, N. A., Nascente, P. A. P., & Kuri, S. E. (2006). Corrosion behavior of supermartensitic stainless steel in aerated and CO2-saturated synthetic seawater. Materials Science and Engineering: A, 428(1-2), 73-79.
48. Hansen, C. M. (1995). New developments in corrosion and blister formation in coatings. Progress in organic coatings, 26(2-4), 113-120.
49. Subramanian, S. (2017). Anticorrosive coatings at high temperatures and high pressures (Master's thesis). Denmark technical University (DTU), Copenhagen.
50. Lacombre, C. V., Bouvet, G., Trinh, D., Mallarino, S., & Touzain, S. (2017). Water uptake in free films and coatings using the Brasher and Kingsbury equation: a possible explanation of the different values obtained by electrochemical Impedance spectroscopy and gravimetry. Electrochimica Acta, 231, 162-170.
51. Apicella, A., Nicolais, L., & De Cataldis, C. (1985). Characterization of the morphological fine structure of commercial thermosetting resins through hygrothermal experiments. In

Characterization of polymers in the solid state I: Part A: NMR and other spectroscopic methods Part B: mechanical methods (pp. 189-207). Springer, Berlin, Heidelberg.

52. Johncock, P., & Tudgey, G. F. (1986). Some Effects of Structure, Composition and Cure on the Water Absorption and Glass Transition Temperature of Amine-cured Epoxies. British polymer journal, 18(5), 292-302.
53. Zhou, J., & Lucas, J. P. (1999). Hygrothermal effects of epoxy resin. Part I: the nature of water in epoxy. Polymer, 40(20), 5505-5512.
54. Zhou, J., & Lucas, J. P. (1999). Hygrothermal effects of epoxy resin. Part II: variations of glass transition temperature. Polymer, 40(20), 5513-5522.